

Cryogenic-Temperature Thermodynamically Suppressed and Strongly Confined CsPbBr₃ Quantum Dots for Deeply Blue Light-Emitting Diodes

Jingjing Cao, Cheng Yan, Chao Luo, Wen Li, Xiankan Zeng, Zhong Xu, Xuehai Fu, Qing Wang, Xiang Chu, Haichao Huang, Xiaoyun Zhao, Jun Lu,* and Weiqing Yang*

Suppressing the naturally ultrafast nucleation and growth rates of perovskite nanocrystals is a big challenge to develop high-performance deeply blue perovskite light-emitting diodes. Here, a cryogenic temperature thermodynamically suppressed synthetic strategy using liquid nitrogen is designed to obtain ultrasmall CsPbBr₃ quantum dots (QDs; ≈3 nm). Due to its strong confinement effect, the as-obtained CsPbBr₃ QDs present strong deeply blue emission (≈460 nm) with a high quantum yield value of up to 98%, a large exciton binding energy of 301.6 meV, and excellent spectra stability for 60 d under atmosphere environment. This unprecedented regime indicates that cryogenic temperature can eliminate pre-existing trap states and suppress the nonradiative process. Besides, the resultant perovskite light-emitting diodes based on ultrasmall CsPbBr₃ QDs show deeply blue emission (≈ 460 nm) with a Commission Internationale de l'Éclairage (CIE) color coordinate of (0.145, 0.054), better than the blue National Television Standards Committee (NTSC) standard. Evidently, this cryogenic temperature synthetic strategy will pave the way for the large-scale synthesis of the strongly confined ultrasmall quantum dots systems and open the door for the development of next generation solid-state lighting and displays.

1. Introduction

Lead halide perovskite nanocrystals (NCs), naturally owning the excellent emission properties, simple chemical synthesis, high photoluminescence quantum yields (PLQY) and defect

Dr. J. J. Cao, Dr. C. Yan, Dr. C. Luo, Dr. W. Li, X. K. Zeng, Dr. Z. Xu, Dr. X. H. Fu, Dr. Q. Wang, Dr. X. Chu, Dr. H. C. Huang, Prof. J. Lu, Prof. W. Q. Yang

Key Laboratory of Advanced Technologies of Materials
(Ministry of Education)


School of Materials Science and Engineering
State Key Laboratory of Traction Power

Southwest Jiaotong University
Chengdu 610031, P. R. China

E-mail: junlyuprc@hotmail.com; wqyang@swjtu.edu.cn

Prof. X. Y. Zhao

College of Optoelectronic Engineering
Chengdu University of Information Technology
Chengdu 610225, P. R. China

 The ORCID identification number(s) for the author(s) of this article can be found under <https://doi.org/10.1002/adom.202100300>.

DOI: 10.1002/adom.202100300

tolerance nature, have been extensively employed to develop high-performance perovskite light-emitting diodes (PeLEDs) for next generation solid-state lighting and display applications.^[1–11] Currently, although great breakthroughs have been made in external quantum efficiency of the near-infrared (21.6%), red (21.3%) and green (20.3%) PeLEDs,^[12–16] the blue PeLEDs still lag behind these counterparts, badly impeding the widely practical applications of PeLEDs-based solid-state lighting and full-color displays.^[17–19] In view of this, both composition engineering and dimensionality engineering have been applied to gradually improve blue PeLEDs performances.^[20–27] However, their emission wavelengths with a range of 475–490 nm are usually difficult to meet the deeply blue emitter (≈460 nm) requirements of next generation solid-state lighting and displays. In this regard, the mixed Br/Cl based anion substitution strategy can achieve the deeply blue emission^[28,29] but usually suffers from phase

separation and ion migration,^[17] naturally resulting in low efficiency and short lifetime of device performances. Recently, 2D CsPbBr₃ PeLEDs with strong quantum confinement in a single dimension has been proved to effectively improve the above performance of deeply blue emission (near to 465 nm).^[30,31] Therefore, to obtain the strongly confined CsPbBr₃ quantum dots (QDs) in 3D by further lowering their size (<5 nm) would have great potential for the shorter emission wavelength, and the higher efficiency of blue PeLEDs. Unfortunately, owing to the ultrafast nucleation and growth rates of CsPbX₃ perovskite nanocrystals, it is challenging to obtain the strongly confined CsPbBr₃ QDs in 3D. The ultrafast nucleation and growth rates originate from intrinsic low formation energy and soft ionic lattice structures.^[32]

Herein, we aim to address this issue by proposing a cryogenic-temperature thermodynamically suppressed (CTTS) synthetic strategy that fully suppresses the ultrafast nucleation and growth rates, resulting in the formation of ultrasmall CsPbBr₃ QDs with a large exciton binding energy as high as 301.6 meV. The as-obtained CsPbBr₃ QDs show strong deeply blue emission of 460 nm with a high quantum yield of up to

98%, and excellent spectra stability for 60 d. Benefiting from the excellent properties of ultrasmall CsPbBr₃ QDs, deeply blue pure bromide PeLEDs with a Commission Internationale de l'Éclairage (CIE) color coordinate of (0.145, 0.054) are achieved, which are better than the blue National Television Standards Committee (NTSC) standard. Unambiguously, this CTTS synthetic strategy will open a way for the large-scale synthesis of the strongly confined ultrasmall quantum dots systems and will greatly promote the rapid development of next generation solid-state lighting and displays.

2. Results and Discussions

2.1. Processing and Optical Characteristics Analysis

Figure 1a and Video S1 in the Supporting Information schematically show the process of CTTS synthetic strategy. Briefly, a certain volume of liquid nitrogen (LN) is quickly poured into the mixed solution including toluene and HBr for the purpose of abruptly lower the synthetic temperature (Figure 1a, I). The prepared precursor solution consisting of CsBr, PbBr₂, and N,N-dimethylformamide (DMF) is rapidly injected before the solution solidify (Figure 1a, II). The optimal timing is at 25 s for

injecting precursor solution (Figure S1, Supporting Information). Such low synthetic temperature can effectively suppress the ultrafast nucleation and growth rates of CsPbX₃ perovskite nanocrystals. Besides, the chemically inert LN can provide the excellent water-oxygen-inhibited environment. In order to investigate the thermodynamically suppressed effect of LN, we compare a control sample prepared at room temperature (RT). Deeply blue (LN-treated) and green (RT-controlled) solutions are observed under UV light (Figure S2 and Video S2, Supporting Information). LN-treated sample shows a band edge absorption peak at 455 nm and a sharp emission peak at 466 nm with a narrow full-width at half-maximum (FWHM) of 12 nm, indicating a narrow size distribution (Figure 1b). In contrast, the RT-controlled sample exhibits a longer excitonic absorption peak centered at 485 nm and a light green emission peak at 500 nm with a broader FWHM of 27 nm (Figure 1d). According to absorption Tauc plots, the optical bandgap of the LN-treated and the RT-controlled samples are calculated to be 2.67 and 2.438 eV, respectively (Figure S3, Supporting Information). The emission peak of LN-treated CsPbBr₃ colloidal solution shows a remarkable blueshift of 34 nm, evidently revealing the appearance of strong quantum confinement.

Besides, the Stokes shift value of LN-treated sample is much smaller than that of the RT-controlled CsPbBr₃, reasonably

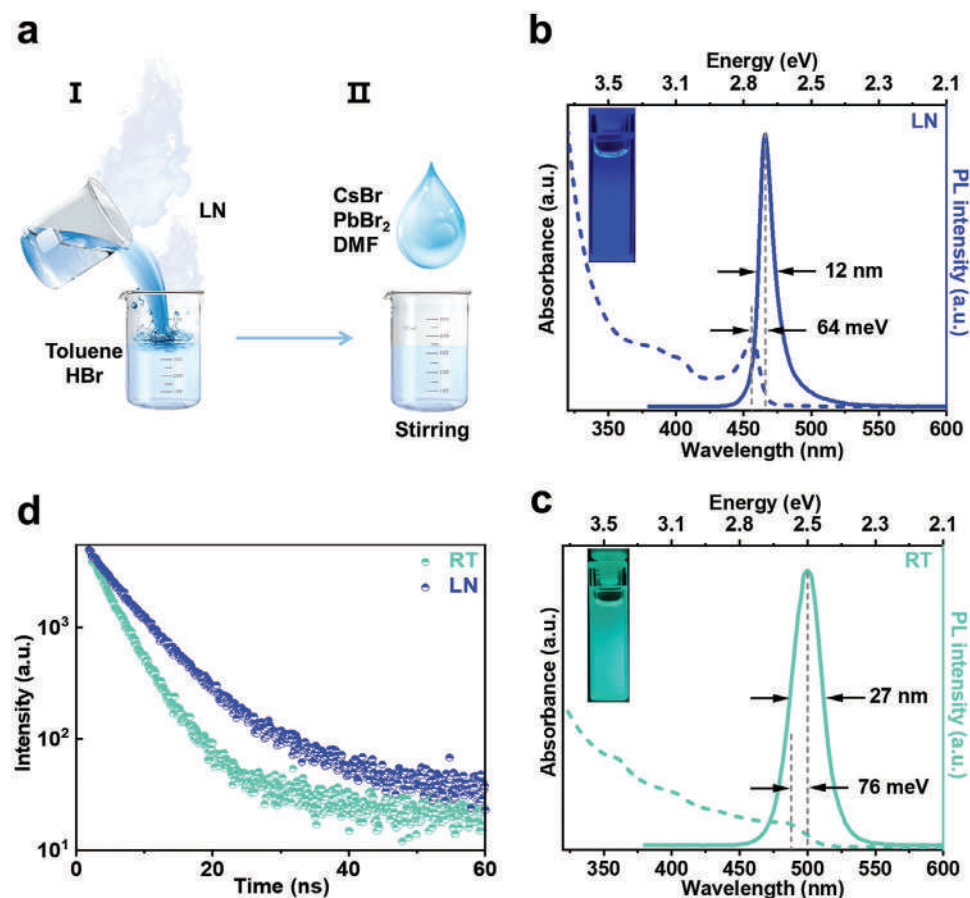


Figure 1. Processing and optical characteristics of CsPbBr₃ perovskites. a) Schematically showing LN-treated solution-processed CsPbBr₃ perovskites. Absorption and photoluminescence spectra of b) the LN-treated and d) the RT-controlled CsPbBr₃ solutions. c) Time-resolved PL (TRPL) decay curves of LN treated and the control (RT) CsPbBr₃ colloidal solutions.

indicating a direct excitation recombination process.^[33] By using biexponential decay functions fitting, the average PL lifetime of LN-treated sample (6.248 ns) is longer than the RT-controlled sample (3.573 ns), pointing to substantially reduced trap states due to CTTS effect (Figure 1c). Further, the PLQY value of LN-treated sample is as high as 98%, dramatically higher than RT-controlled sample (87%) (Figure S4, Supporting Information), which again reveals a lower trap density and less nonradiative recombination of LN-treated sample. Also, the LN-treated sample with abruptly tenfold-dropped nonradiative rate constant k_{nr} (Table S1, Supporting Information) and a smaller Urbach energy (E_u) (Figure S5, Supporting Information) than the RT-controlled sample fully reveals the excellent passivation effect of cryogenic temperature on the nonradiative trap centers. Moreover, the spectra stability is an important indicator to evaluate the performance of CsPbBr₃ QDs. After storage in air without any additional processing for 10 d, the LN-treated sample remains 88% PL emission intensity (Figure S6, Supporting Information). Obviously, the stability of LN-treated sample is the mostly same with the RT-controlled sample within 10 d. In addition, the emission peaks position of LN-treated sample could keep unchanged for 60 d (Figure S7, Supporting Information), the strongest stability among strongly confined CsPbBr₃ QDs with deeply blue emission so far, demonstrating the effectiveness of CTTS synthetic strategy.

2.2. Structural and Morphological Analysis

The X-ray powder diffraction (XRD) results (Figure S8, Supporting Information) indicate the cubic CsPbBr₃ (Joint Committee on Powder Diffraction Standards No. powder diffraction files 75-0412) of both LN-treated and RT-controlled samples. In comparison with the RT-controlled sample, the diffraction peak positions of LN-treated sample slightly shift to higher degrees [$\Delta 2\theta \approx 0.56^\circ$ for the (100) and $\Delta 2\theta \approx 0.31^\circ$ for the (200) planes], obviously revealing the lattice contraction as a result of CTTS effect. For the RT-controlled sample, the diffraction angles in the range of 18.33° – 28.35° can be assigned to the characteristic diffraction peak of the existed ligands (oleic acid or oleylamine). As shown in Figure 2a,b, the transmission electron microscope (TEM) images of LN-treated sample show ultrasmall QDs with an average diameter of 3.34 nm, much lower than the intrinsic exciton bohr radius of CsPbBr₃ (≈ 7 nm), further verifying the formation of strong quantum confinement mentioned above. In contrast, the RT-controlled sample exhibits much larger and inhomogeneous rectangular morphology with a lateral dimension of 10.58 nm (Figure 2e,f). From Figure 2c,g, the clear lattice fringes reveal the excellent crystallinity. The corresponding interplanar distances of (210), (200), and (100) are 0.2688, 0.2938, and 0.5667 nm, respectively, which is in good agreement with the XRD results (Figure S8, Supporting Information). The selected area electron diffraction (SAED) patterns are also detected to further confirm the phases of the nanocrystals in Figure 2d,h.

As illustrated in Figure 2i, Fourier transform infrared (FTIR) spectroscopy spectrum of LN-treated sample keeps almost unchanged in comparison with the RT-controlled sample, proving that the strong quantum confinement should be originated from CTTS effect not the ligands. For the Cs 3d, Pb 4f, and Br 3d

X-ray photoelectron spectra (XPS) of the RT-controlled sample (Figure 2j–l), the higher binding energies of LN-treated sample fully demonstrate the lattice contraction from the decreasing Cs–Br and Pb–Br bond lengths. These reasonably indicate that CTTS effect is conducive to increasing the Cs–Br and Pb–Br interactions and forming stable Cs–Br and Pb–Br bonds.^[34–36] Therefore, this CTTS synthetic strategy has been indeed proved to effectively prepare strongly confined ultrasmall CsPbBr₃ QDs with excellent optical performance and structure stability.

The key to rapidly suppress the superfast nucleation and growth of perovskite nanocrystal for ultrasmall CsPbBr₃ QDs is to greatly decrease the antisolvent (toluene)-reacted temperature to induce the supersaturation of precursors. As schematically depicted in Figure 2m, the overall nucleation and crystal growth process can be explained by LaMer–Dinegar model.^[37] When the monomers reach a critical concentration, the nucleation begins to occur only in a short time. The lower reaction temperature, the slower the rates of nucleation and growth. In our work, the monomer concentration of the LN-treated sample is lower than that of the RT-controlled sample due to the lower solubility of the mixed solution consisting of Cs⁺, [PbBr₆]⁴⁻ at cryogenic temperature, which plays a crucial role in the nucleation and growth kinetics.^[38] Hence, it takes a longer time to nucleate and grow into particles to ultimately achieve strongly confined ultrasmall CsPbBr₃ QDs. This can be proved by the experiment phenomena in the photographs of Figure S9 in the Supporting Information. The solution sequentially presented milk-white, pale green, and green. The whole process took as long as 60 min, far slower than the previously reported nucleation and growth kinetics works.^[39,40] While for RT-controlled sample, the rapidly reacted process exhibited the color instantaneous-changing from colorless to green, and quickly formed the larger grain sizes. Compared with liquid nitrogen and RT, dry ice ($\approx 70^\circ\text{C}$) and ice water (0°C) had been used to obtain intermediate temperature (Figure S10, Supporting Information). The emission peaks were located at 472 and 494 nm, respectively, which indicated that emission wavelength increased with temperature rising. With the rising of temperature, nucleation and growth rates of CsPbBr₃ NCs would be accelerated leading to the increase of grain sizes. As demonstrated in Figure 2n, the lower reaction energy at cryogenic temperature can suppress the formation of defects, which is in favor of improving optical performance and structure stability of ultrasmall QDs.

2.3. Photoexcited Carrier Dynamics Analysis

To gain more insight into the mechanism behind intriguing photophysical properties induced by cryogenic temperature, photoexcited carrier dynamics through femtosecond (fs) time-resolved transient absorption (TA) spectrum measurements were monitored. In general, the photoexcitation wavelength of 365 nm is sufficient for realizing interband transition of both samples. Figure 3a,d shows a narrow negative probe bleaching (PB) signal at around 452 nm for the LN-treated sample, reaching its maximum value with only a 1 ps delay. This PB peak is consistent with the steady absorption peak and is evidently proved to be ascribed to the ground state depopulation.^[41] It is worth noting that the stimulated emission would bring about

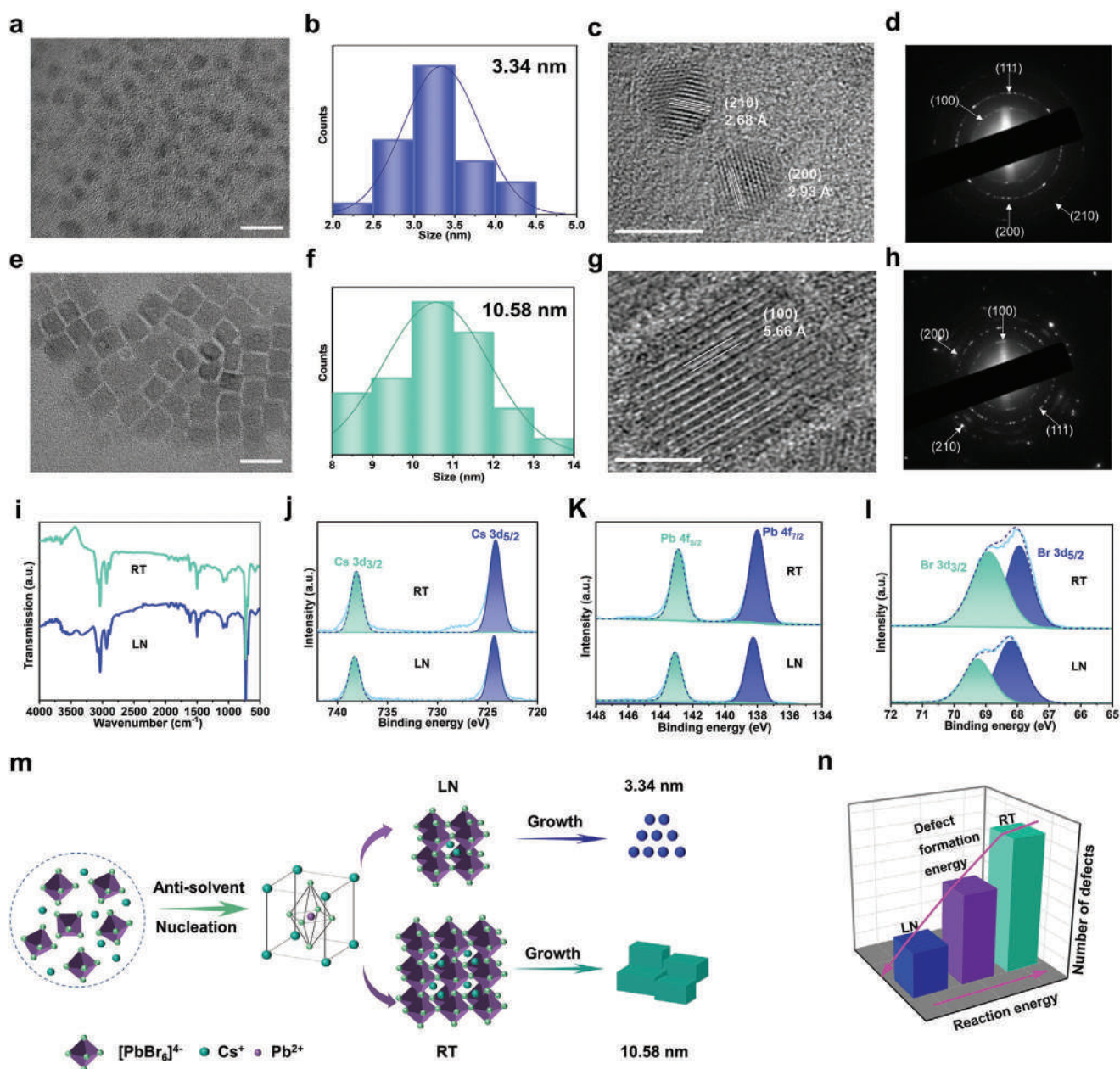


Figure 2. Structural and morphological properties of CsPbBr₃ perovskites. Transmission electron microscope (TEM) and high-resolution TEM (HRTEM) images of a,c) LN-treated (scale bars: 10 and 5 nm, respectively) and e,g) the RT-controlled (scale bars: 20 and 5 nm, respectively) samples. b,f) The corresponding statistics of the size distribution and d,h) SAED patterns. i) FTIR spectra of LN-treated and RT-controlled samples. XPS spectra of j) Cs 3d, k) Br 3d, and l) Pb 4f of LN-treated and RT-controlled samples. m) Schematic diagram of the nucleation and crystal growth process. n) Schematic illustration of cryogenic temperature thermodynamically suppressed effect.

a small contribution to this negative bleach signal.^[42] Besides, there are two positive photoinduced absorption (PA): one is in the 425–444 nm region originated from the lowest excitonic state (labeled as PA1), as its formation time matches well with the intraband relaxation time; the other is in the 462–481 nm region arising from hot carrier absorption (labeled as PA2), as its decay time is identical to the formation time of PB. By contrast, as shown in Figure 3b,e, the RT-controlled sample obviously presents the broader exciton bleaching peaks between 457 and 531 nm (labeled as PB1), revealing the instability of carrier

dynamics. The strongest negative bleaching signals appear at the delay time of 10 ps (≈ 496 nm), meanwhile, a weak negative signal toward lower energy also appear like an extended tail at around 517 nm, which is derived from the state-filling of trap states.^[43,44] With the delay time growing, the bleaching peaks are obviously redshifted and then evidently blueshifted, further demonstrating the instability of carrier dynamics for the RT-controlled sample. Likewise, two positive signals are in the 438–470 nm (PA1) and 505–540 nm (PA2) region, respectively. Furthermore, the bleach recovery dynamics for the

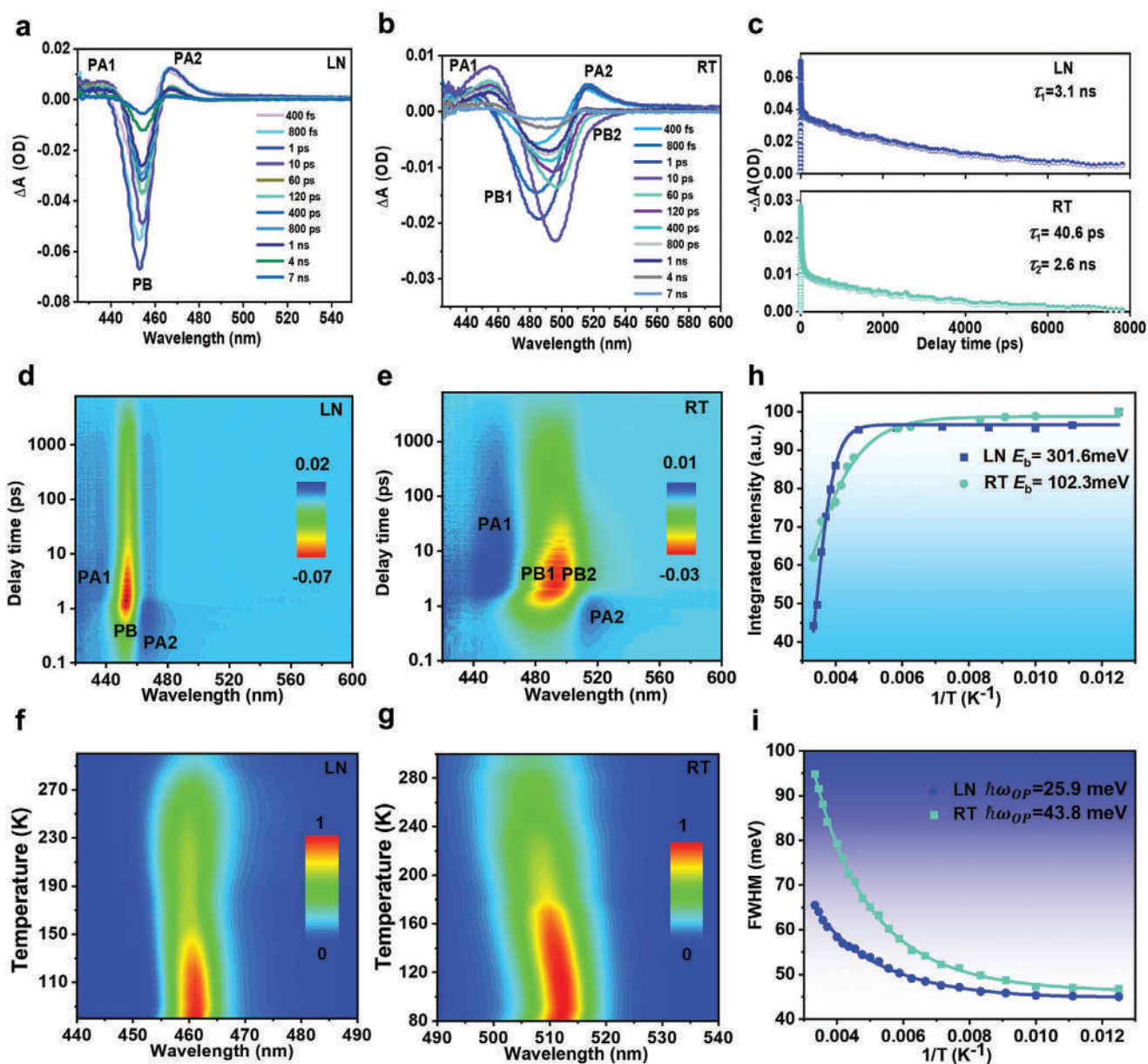


Figure 3. Photoexcited carrier dynamics analysis. The fs-TA spectra of a) LN-treated and b) the RT-controlled samples at different delay time. c) Comparison of TA bleach recovery kinetics of the LN-treated monitored at 454 nm and the RT-controlled samples (RT) monitored at 494 nm. Pseudocolor (ΔA) representation of transient absorption spectra of d) LN-treated and e) the RT-controlled samples. Wavelength of pumping laser = 365 nm; pulse energy density $\approx 28 \mu\text{J cm}^{-2}$. The temperature-dependent PL spectra of f) LN-treated and g) the RT-controlled samples in the range from 80 to 300 K excited at 365 nm. h) Integrated PL intensity and i) FWHM of the LN-treated and RT-controlled samples (RT) as a function of reciprocal temperature.

RT-controlled sample is fitted by a biexponential decay model with ultrafast component (40.6 ps) stemming from carrier trapping and a longer component (2.6 ns) arising from the recombination process (Figure 3c).^[45] However, the single-exponential fitting is quite suitable for exploring the kinetics of exciton relaxation of the LN-treated sample with a long component (3.1 ns). This long component is much slower than the RT-controlled sample, which is in good agreement with the PL lifetime of free excitons (Figure 1d). The above results proved that the cryogenic temperature could eliminate pre-existing trap states and suppress the nonradiative process.

To deeply understand the exciton dynamics of two samples, we also carried out the temperature dependence of PL measurements in the temperature ranges from 80 to 300 K in Figure 3f,g, and Figure S11 in the Supporting Information. In view of enhanced thermally activated nonradiative recombination process at higher temperature, the band-edge PL intensities of two samples progressively decrease.^[46] In addition, the PL spectra of the two samples are absolutely symmetrical over the entire temperature range, revealing the nonexistence of a structural phase transition.^[47] The FWHM of the LN-treated sample (788 nm) at 80 K is narrower than that of the RT-controlled sample (9.86 nm)

(Figure S12, Supporting Information), which should be attributed to strong exciton recombination behavior with few structural defect states.^[46] Obviously, the emission peak position of the LN-treated sample has a subtle change with the increasing temperature, yet it shows a remarkable blueshift for the RT-controlled sample (Figure S11, Supporting Information). This fully demonstrates the cryogenic temperature could effectively promote the structure stability of ultrasmall CsPbBr₃ QDs. This blueshift phenomenon is ascribed to lattice expansion, leading to the decrease of valence band maxima potential energy and the increase of the conduction band minima potential energy.^[48] In Figure 3h, the exciton binding energy (E_b) of the LN-treated sample is as high as 301.6 meV, much higher than that of the RT-treated sample (102.3 meV). Such high exciton binding energy adequately confirms that the PL emissions of strongly confined ultrasmall CsPbBr₃ QDs mainly take place via exciton recombination instead of the recombination of free electrons and holes.^[49,50] Moreover, the temperature-independent PL line width has an important influence on the excitonic PL emissions and can provide information about the interaction of excitons with optical or acoustic phonons. As presented in Figure 3f, the optical phonon energy ($\hbar\omega_{OP}$) of the LN-treated sample (25.9 meV) is much lower than that of the RT-controlled sample (43.8 meV), indicative of the stronger excitonic emission behavior, basically close to the results for CsPbX₃ (X = Cl, Br, I) perovskite nanocrystals ($\approx 16\text{--}40$ meV).^[51]

2.4. Bandgap Tunability

After the last step of centrifugation, the LN-treated samples were diluted with toluene volume of 4, 8, 16, and 20 mL, labeled as 470, 466, 463, and 460 nm, respectively. In Figure 4a, the sample (470 nm) has a broader absorption range from 441 to 460 nm, while the other three samples possess the narrower absorption peaks, almost overlapping at 453 nm. All the samples obviously present the strong pure blue emissions ranging from 460 to 470 nm (Figure 4b), and their corresponding CIE color coordinates match well with the strict Rec. 2020 standard for next-generation color displays applications (Figure 4c). Their emission wavelengths present remarkable blueshift with strong dilutions, which is consistent with previous report.^[52] From Figure 4d, the PL lifetime will increase with an increase of emission wavelength. Detailed information with respect to emission wavelength, FWHM, CIE color coordinate and PL lifetime are shown in Table S2 in the Supporting Information. The larger toluene solution volume, the lower concentration of final sample, leading to the partially peeling off of organic ligands from CsPbBr₃ QDs surface and then gradually reducing particle sizes can controllably result in the decreasing emission wavelength from 470 to 460 nm. Although the solution gets colorless and transparent when the toluene volume reaches up to 20 mL, it can

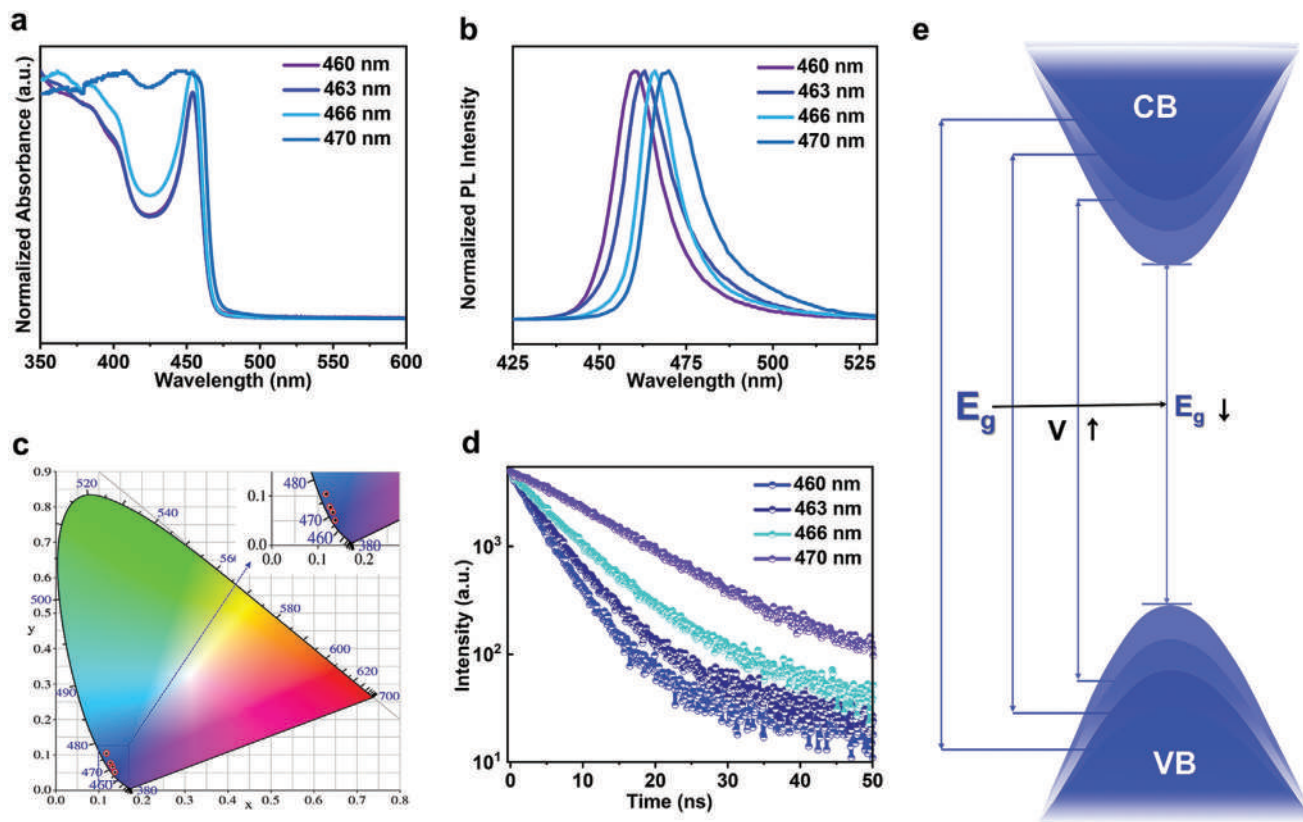


Figure 4. Bandgap-tunable deeply blue CsPbBr₃ QDs. a) Optical absorption spectra and b) the PL spectra of four samples diluted with different volumes of toluene. c) CIE color coordinates of four samples. Inset (c): Enlarged rectangular frame picture. d) Time-resolved photoluminescence (TRPL) decay of four samples. e) Schematic illustration of bandgap tunability. Note: All the samples were treated with LN, except diluted with different volumes of toluene after centrifugation.

still display the remarkably strong blue emission under UV light (Video S3, Supporting Information). Noted, the uniform and clear QD solution has no precipitation during the whole dispersion process, presenting the excellent dispersibility. Figure 4e presents the schematic illustration of bandgap tunability. The increased toluene volume can lead to a blueshifted emission peak and widened bandgap. Compared with conventional halogen ion exchange method, this solvent dilution strategy is simple and effective to achieve tunable bandgap.

2.5. Pure Bromide Deeply Blue PeLED Performance

Encouraged by the outstanding performance of LN-treated sample, we thus fabricated deeply blue PeLEDs using the ultrasmall CsPbBr₃ QDs, as the device structure indicated in Figure 5a. Figure 5b displays the EL spectra of blue PeLED under different bias voltages (2.5–4.5 V). Notably, the electroluminescent (EL) intensity rises monotonically with increasing the bias voltages, which reveals that the undesirable non-radiative recombination or series resistance would fail to increase proportionally as the voltage increases.^[53] As shown in Figure 5c, the EL spectrum of deeply blue PeLED is consistent

with PL spectrum with a symmetric emission peak centered at ≈460 nm and a narrow FWHM of 17.8 nm, giving deeply blue emission with high color purity. This deeply blue emission corresponds to the CIE color coordinate of (0.145, 0.054), better than the blue NTSC standard of (0.14, 0.08) (Figure 5d).

3. Conclusion

In summary, a CTTS synthetic strategy employing liquid nitrogen is proposed to successfully prepare strongly confined ultrasmall CsPbBr₃ QDs (≈3 nm) with a large exciton binding energy of 301.6 meV. This strongly confined effect enables ultrasmall CsPbBr₃ QDs with strong deeply blue emission of ≈460 nm, high PLQY value of up to 98% and excellent spectra stability of 60 d under atmosphere environment. Temperature-dependent PL and TA measurements indicate cryogenic temperature could eliminate pre-existing trap states and suppress the nonradiative process. Finally, PeLED devices using ultrasmall CsPbBr₃ QD as active layer were fabricated, exhibiting deeply blue emission (≈460 nm) with a CIE color coordinate of (0.145, 0.054), better than the blue NTSC standard. Undoubtedly, this promising work will contribute an effective strategy

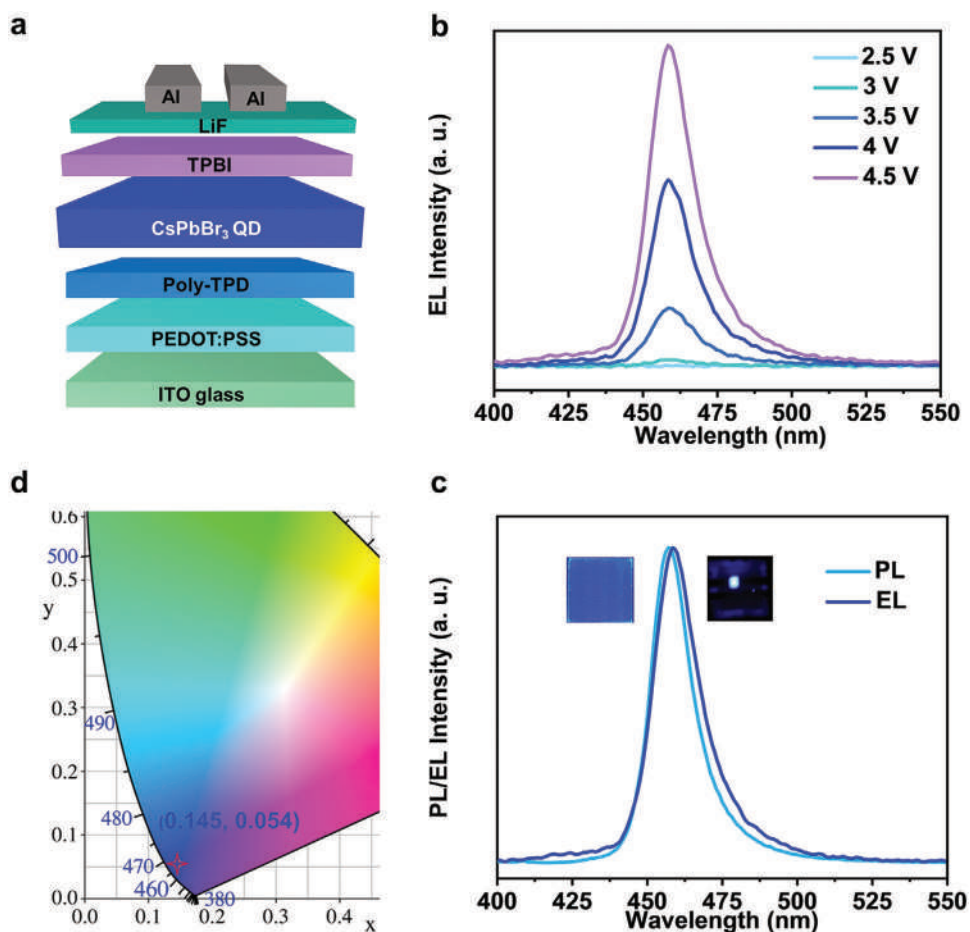


Figure 5. Pure bromide deeply blue PeLED performances based on ultrasmall CsPbBr₃ QDs. a) Device structure. b) EL spectra under various bias voltages. c) EL and PL spectra of deeply blue PeLED. Inset (c): A photograph of a film under UV irradiation (left) and a photograph of a working blue device (right). d) CIE value of the EL spectrum of deeply blue LED.

for outstanding performance and stable deeply blue pure bromide perovskite materials toward next generation solid-state lighting and displays applications.

Supporting Information

Supporting Information is available from the Wiley Online Library or from the author.

Acknowledgements

J.J.C. and C.Y. contributed equally to this work. This work was financially supported by the National Natural Science Foundation of China (No. 52073237) and by Young Scientific and Technological Innovation Research Team Funds of Sichuan Province (Nos. 20CXTD0106 and 2019YFG0292). The authors gratefully acknowledge ceshigo (www.ceshigo.com) for providing testing services. The authors are thankful to Analytical and Testing Center of Southwest Jiaotong University for supporting the XRD and TEM measurements.

Conflict of Interest

The authors declare no conflict of interest.

Data Availability Statement

Research data are not shared.

Keywords

cryogenic temperature, CsPbBr₃ quantum dots, perovskite light-emitting diodes, perovskite nanocrystals, strong confinement, thermodynamically suppressed

Received: February 14, 2021

Revised: April 21, 2021

Published online:

- [1] X. H. He, Y. C. Qiu, S. H. Yang, *Adv. Mater.* **2017**, *29*, 1700775.
- [2] J. M. Huang, M. L. Lai, J. Lin, P. D. Yang, *Adv. Mater.* **2018**, *30*, 1802856.
- [3] M. V. Kovalenko, L. Protesescu, M. I. Bodnarchuk, *Science* **2017**, *358*, 745.
- [4] G. P. Li, H. Wang, T. Zhang, L. F. Mi, Y. G. Zhang, Z. P. Zhang, W. J. Zhang, Y. Jiang, *Adv. Funct. Mater.* **2016**, *26*, 8478.
- [5] G. R. Li, F. W. R. Rivarola, N. J. L. K. Davis, S. Bai, T. C. Jellicoe, F. de la Pena, S. C. Hou, C. Ducati, F. Gao, R. H. Friend, N. C. Greenham, Z. K. Tan, *Adv. Mater.* **2016**, *28*, 3528.
- [6] X. M. Li, D. J. Yu, F. Cao, Y. Gu, Y. Wei, Y. Wu, J. Z. Song, H. B. Zeng, *Adv. Funct. Mater.* **2016**, *26*, 5903.
- [7] C. Luo, W. Li, J. Fu, W. Q. Yang, *Chem. Mater.* **2019**, *31*, 5616.
- [8] C. Luo, C. Yan, W. Li, F. J. Chun, M. L. Xie, Z. H. Zhu, Y. Gao, B. L. Guo, W. Q. Yang, *Adv. Funct. Mater.* **2020**, *30*, 2000026.
- [9] J. Shamsi, A. S. Urban, M. Imran, L. De Trizio, L. Manna, *Chem. Rev.* **2019**, *119*, 3296.
- [10] M. L. Xie, H. Liu, F. J. Chun, W. Deng, C. Luo, Z. H. Zhu, M. Yang, Y. M. Li, W. Li, W. Yan, W. Q. Yang, *Small* **2019**, *15*, 1901994.
- [11] X. Y. Zhang, X. Bai, H. Wu, X. T. Zhang, C. Sun, Y. Zhang, W. Zhang, W. T. Zheng, W. W. Yu, A. L. Rogach, *Angew. Chem., Int. Ed.* **2018**, *57*, 3337.
- [12] K. B. Lin, J. Xing, L. N. Quan, F. P. G. de Arquer, X. W. Gong, J. X. Lu, L. Q. Xie, W. J. Zhao, D. Zhang, C. Z. Yan, W. Q. Li, X. Y. Liu, Y. Lu, J. Kirman, E. H. Sargent, Q. H. Xiong, Z. H. Wei, *Nature* **2018**, *562*, 245.
- [13] Y. Cao, N. N. Wang, H. Tian, J. S. Guo, Y. Q. Wei, H. Chen, Y. F. Miao, W. Zou, K. Pan, Y. R. He, H. Cao, Y. Ke, M. M. Xu, Y. Wang, M. Yang, K. Du, Z. W. Fu, D. C. Kong, D. X. Dai, Y. Z. Jin, G. Q. Li, H. Li, Q. M. Peng, J. P. Wang, W. Huang, *Nature* **2018**, *562*, 249.
- [14] T. Chiba, Y. Hayashi, H. Ebe, K. Hoshi, J. Sato, S. Sato, Y. J. Pu, S. Ohisa, J. Kido, *Nat. Photonics* **2018**, *12*, 681.
- [15] Y. Shen, M. N. Li, Y. Q. Li, F. M. Xie, H. Y. Wu, G. H. Zhang, L. Chen, S. T. Lee, J. X. Tang, *ACS Nano* **2020**, *14*, 6107.
- [16] W. D. Xu, Q. Hu, S. Bai, C. X. Bao, Y. F. Miao, Z. C. Yuan, T. Borzda, A. J. Barker, E. Tyukalova, Z. J. Hu, M. Kawecki, H. Y. Wang, Z. B. Yan, X. J. Liu, X. B. Shi, K. Uvdal, M. Fahlman, W. J. Zhang, M. Duchamp, J. M. Liu, A. Petrozza, J. P. Wang, L. M. Liu, W. Huang, F. Gao, *Nat. Photonics* **2019**, *13*, 418.
- [17] Z. C. Li, Z. M. Chen, Y. C. Yang, Q. F. Xue, H. L. Yip, Y. Cao, *Nat. Commun.* **2019**, *10*, 1027.
- [18] P. Vashishtha, M. Ng, S. B. Shivarudraiah, J. E. Halpert, *Chem. Mater.* **2019**, *31*, 83.
- [19] C. H. A. Li, Z. C. Zhou, P. Vashishtha, J. E. Halpert, *Chem. Mater.* **2019**, *31*, 6003.
- [20] Y. T. Dong, Y. K. Wang, F. L. Yuan, A. Johnston, Y. Liu, D. X. Ma, M. J. Choi, B. Chen, M. Chekini, S. W. Baek, L. K. Sagar, J. Fan, Y. Hou, M. J. Wu, S. Lee, B. Sun, S. Hoogland, R. Quintero-Bermudez, H. Ebe, P. Todorovic, F. Dinic, P. C. Li, H. T. Kung, M. I. Saidaminov, E. Kumacheva, E. Spiecker, L. S. Liao, O. Voznyy, Z. H. Lu, E. H. Sargent, *Nat. Nanotechnol.* **2020**, *15*, 668.
- [21] J. Xing, Y. B. Zhao, M. Askerka, L. N. Quan, X. W. Gong, W. J. Zhao, J. X. Zhao, H. R. Tan, G. K. Long, L. Gao, Z. Y. Yang, O. Voznyy, J. Tang, Z. H. Lu, Q. H. Xiong, E. H. Sargent, *Nat. Commun.* **2018**, *9*, 3541.
- [22] M. K. Gangishetty, S. C. Hou, Q. M. Quan, D. N. Congreve, *Adv. Mater.* **2018**, *30*, 1706226.
- [23] Q. Wang, X. M. Wang, Z. Yang, N. H. Zhou, Y. H. Deng, J. J. Zhao, X. Xiao, P. Rudd, A. Moran, Y. F. Yan, J. S. Huang, *Nat. Commun.* **2019**, *10*, 5633.
- [24] Y. Liu, J. Y. Cui, K. Du, H. Tian, Z. F. He, Q. H. Zhou, Z. L. Yang, Y. Z. Deng, D. Chen, X. B. Zuo, Y. Ren, L. Wang, H. M. Zhu, B. D. Zhao, D. W. Di, J. P. Wang, R. H. Friend, Y. Z. Jin, *Nat. Photonics* **2019**, *13*, 760.
- [25] Y. Shynkarenko, M. I. Bodnarchuk, C. Bernasconi, Y. Berezovska, V. Verteletskiy, S. T. Ochsenbein, M. V. Kovalenko, *ACS Energy Lett.* **2019**, *4*, 2703.
- [26] Z. M. Chu, Y. Zhao, F. Ma, C. X. Zhang, H. X. Deng, F. Gao, Q. F. Ye, J. H. Meng, Z. G. Yin, X. W. Zhang, J. B. You, *Nat. Commun.* **2020**, *11*, 4165.
- [27] Y. Z. Jiang, C. C. Qin, M. H. Cui, T. W. He, K. K. Liu, Y. M. Huang, M. H. Luo, L. Zhang, H. Y. Xu, S. S. Li, J. L. Wei, Z. Y. Liu, H. H. Wang, W. Kim, M. J. Yuan, J. Chen, *Nat. Commun.* **2019**, *10*, 1868.
- [28] G. C. Pan, X. Bai, W. Xu, X. Chen, Y. Zhai, J. Y. Zhu, H. Shao, N. Ding, L. Xu, B. Dong, Y. L. Mao, H. W. Song, *ACS Appl. Mater. Interfaces* **2020**, *12*, 14195.
- [29] X. P. Zheng, S. Yuan, J. K. Liu, J. Yie, F. L. Yuan, W. S. Shen, K. X. Yao, M. Y. Wei, C. Zhou, K. P. Song, B. B. Zhang, Y. B. Lin, M. N. Hedhili, N. Wehbe, Y. Han, H. T. Sun, Z. H. Lu, T. D. Anthopoulos, O. F. Mohammed, E. H. Sargent, L. S. Liao, O. M. Bakr, *ACS Energy Lett.* **2020**, *5*, 793.
- [30] N. Yantara, N. F. Jamaludin, B. Febriansyah, D. Giovanni, A. Bruno, C. Soci, T. C. Sum, S. Mhaisalkar, N. Mathews, *ACS Energy Lett.* **2020**, *5*, 1593.

- [31] S. Yuan, Z.-K. Wang, L.-X. Xiao, C.-F. Zhang, S.-Y. Yang, B.-B. Chen, H.-T. Ge, Q.-S. Tian, Y. Jin, L.-S. Liao, *Adv. Mater.* **2019**, *31*, 1904319.
- [32] K. Miyata, T. L. Atallah, X. Y. Zhu, *Sci. Adv.* **2017**, *3*, e1701469.
- [33] H. Huang, A. S. Susha, S. V. Kershaw, T. F. Hung, A. L. Rogach, *Adv. Sci.* **2015**, *2*, 1500194.
- [34] M. Worku, Y. Tian, C. Zhou, H. Lin, M. Chaaban, L.-j. Xu, Q. He, D. Beery, Y. Zhou, X. Lin, Y.-f. Su, Y. Xin, B. Ma, *Sci. Adv.* **2020**, *6*, eaaz5961.
- [35] J. K. Nam, S. U. Chai, W. Cha, Y. J. Choi, W. Kim, M. S. Jung, J. Kwon, D. Kim, J. H. Park, *Nano Lett.* **2017**, *17*, 2028.
- [36] M. Liu, G. Zhong, Y. Yin, J. Miao, K. Li, C. Wang, X. Xu, C. Shen, H. Meng, *Adv. Sci.* **2017**, *4*, 1700335.
- [37] V. K. LaMer, R. H. Dinegar, *J. Am. Chem. Soc.* **1950**, *72*, 4847.
- [38] M. P. Hendricks, M. P. Campos, G. T. Cleveland, I. Jen-La Plante, J. S. Owen, *Science* **2015**, *348*, 1226.
- [39] Y. T. Dong, T. Qiao, D. Kim, D. Parobek, D. Rossi, D. H. Son, *Nano Lett.* **2018**, *18*, 3716.
- [40] J. F. Leng, T. Wang, X. F. Zhao, E. W. Y. Ong, B. S. Zhu, J. D. Ng, Y. C. Wong, K. H. Khoo, K. Tamada, Z. K. Tan, *J. Phys. Chem. Lett.* **2020**, *11*, 2036.
- [41] V. I. Klimov, D. W. McBranch, *Phys. Rev. Lett.* **1998**, *80*, 4028.
- [42] J. S. Manser, J. A. Christians, P. V. Kamat, *Chem. Rev.* **2016**, *116*, 12956.
- [43] G. C. Xing, M. H. Kumar, W. K. Chong, X. F. Liu, Y. Cai, H. Ding, M. Asta, M. Gratzel, S. Mhaisalkar, N. Mathews, T. C. Sum, *Adv. Mater.* **2016**, *28*, 8191.
- [44] X. X. Wu, M. T. Trinh, D. Niesner, H. M. Zhu, Z. Norman, J. S. Owen, O. Yaffe, B. J. Kudisch, X. Y. Zhu, *J. Am. Chem. Soc.* **2015**, *137*, 2089.
- [45] N. Mondal, A. Samanta, *Nanoscale* **2017**, *9*, 1878.
- [46] Y. Li, Z. F. Shi, S. Li, L. Z. Lei, H. F. Ji, D. Wu, T. T. Xu, Y. T. Tian, X. J. Li, *J. Mater. Chem. C* **2017**, *5*, 8355.
- [47] F. Y. Meng, X. Y. Liu, X. Y. Cai, Z. F. Gong, B. B. Li, W. T. Xie, M. K. Li, D. C. Chen, H. L. Yip, S. J. Su, *Nanoscale* **2019**, *11*, 1295.
- [48] Z. Song, J. Zhao, Q. L. Liu, *Inorg. Chem. Front.* **2019**, *6*, 2969.
- [49] C. X. Sheng, C. Zhang, Y. X. Zhai, K. Mielczarek, W. W. Wang, W. L. Ma, A. Zakhidov, Z. V. Vardeny, *Phys. Rev. Lett.* **2015**, *114*, 116601.
- [50] Y. Jiang, X. Wang, A. L. Pan, *Adv. Mater.* **2019**, *31*, 1806671.
- [51] J. Zhang, Y. Yang, H. Deng, U. Farooq, X. K. Yang, J. Khan, J. Tang, H. S. Song, *ACS Nano* **2017**, *11*, 9294.
- [52] H. Huang, M. W. Feil, S. Fuchs, T. Debnath, A. F. Richter, Y. Tong, L. Z. Wu, Y. O. Wang, M. Doblinger, B. Nickel, *Chem. Mater.* **2020**, *32*, 8877.
- [53] X. Yang, C. Shan, Q. Liu, M. Jiang, Y. Lu, X. Xie, B. Li, D. Shen, *ACS Photonics* **2018**, *5*, 1006.